Chapter 4

Influence of abdominal aortic aneurysm shape on hemodynamics in human aortofemoral arteries: A transient open-loop study

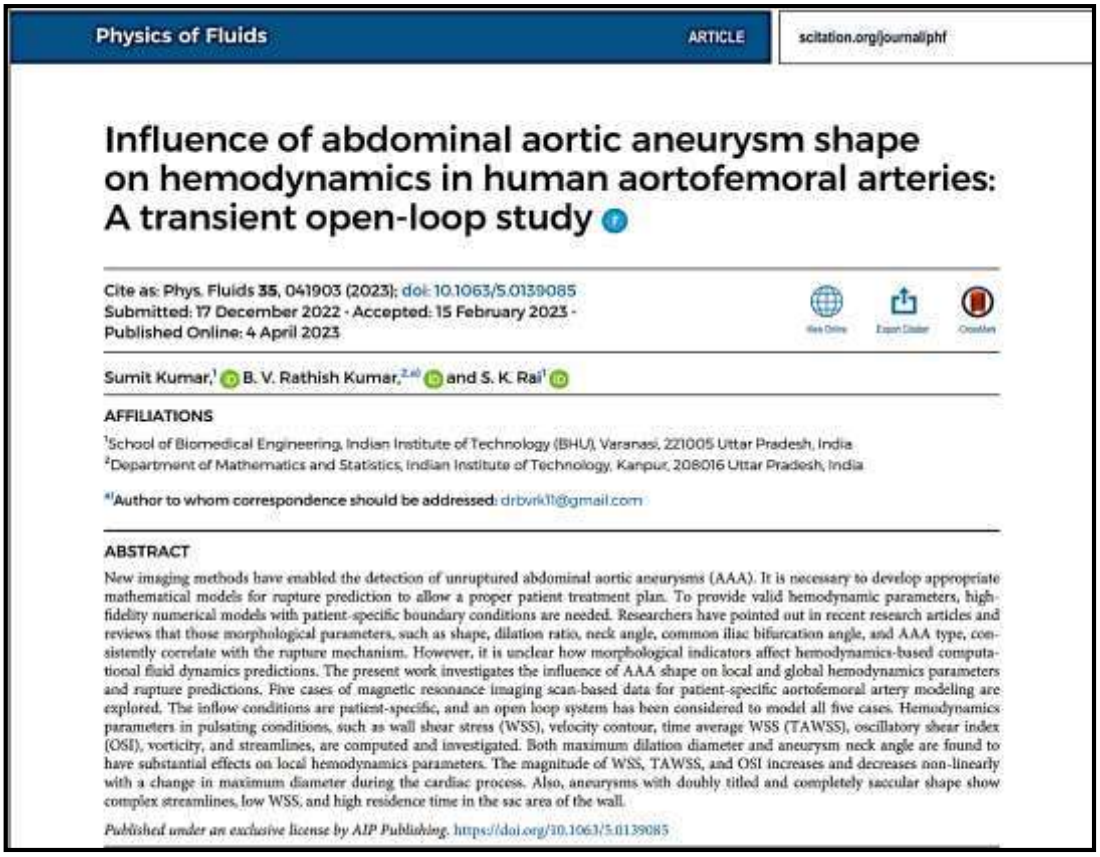

Physics of Fluids ARTICLE scitation.org/journal/phf

Influence of abdominal aortic aneurysm shape on hemodynamics in human aortofemoral arteries: A transient open-loop study

Cite as: Phys. Fluids 35, 041903 (2023); doi: 10.1063/5.0139085
Submitted: 17 December 2022 · Accepted: 15 February 2023 ·
Published Online: 4 April 2023

Sumit Kumar,[1] B. V. Rathish Kumar,[2,a)] and S. K. Rai[1]

AFFILIATIONS

[1]School of Biomedical Engineering, Indian Institute of Technology (BHU), Varanasi, 221005 Uttar Pradesh, India
[2]Department of Mathematics and Statistics, Indian Institute of Technology, Kanpur, 208016 Uttar Pradesh, India

[a)]Author to whom correspondence should be addressed: drbvrk11@gmail.com

ABSTRACT

New imaging methods have enabled the detection of unruptured abdominal aortic aneurysms (AAA). It is necessary to develop appropriate mathematical models for rupture prediction to allow a proper patient treatment plan. To provide valid hemodynamic parameters, high-fidelity numerical models with patient-specific boundary conditions are needed. Researchers have pointed out in recent research articles and reviews that those morphological parameters, such as shape, dilation ratio, neck angle, common iliac bifurcation angle, and AAA type, consistently correlate with the rupture mechanism. However, it is unclear how morphological indicators affect hemodynamics-based computational fluid dynamics predictions. The present work investigates the influence of AAA shape on local and global hemodynamics parameters and rupture predictions. Five cases of magnetic resonance imaging scan-based data for patient-specific aortofemoral artery modeling are explored. The inflow conditions are patient-specific, and an open loop system has been considered to model all five cases. Hemodynamics parameters in pulsating conditions, such as wall shear stress (WSS), velocity contour, time average WSS (TAWSS), oscillatory shear index (OSI), vorticity, and streamlines, are computed and investigated. Both maximum dilation diameter and aneurysm neck angle are found to have substantial effects on local hemodynamics parameters. The magnitude of WSS, TAWSS, and OSI increases and decreases non-linearly with a change in maximum diameter during the cardiac process. Also, aneurysms with doubly titled and completely saccular shape show complex streamlines, low WSS, and high residence time in the sac area of the wall.

Published under an exclusive license by AIP Publishing. https://doi.org/10.1063/5.0139085

Chapter 4

Influence of abdominal aortic aneurysm shape on hemodynamics in human aortofemoral arteries: A transient open-loop study

4.1 Introduction

Abdominal aortic aneurysms (AAAs) are described as an expansion of the abdominal aorta of 1.5 times or more. Aneurysms in the abdominal aorta are the most common type and can cause severe consequences without warning. Distended abdominal aortic aneurysms (AAAs) have a mortality rate of up to 75%, and vascular disease is a leading cause of death globally (Aggarwal et al., 2011; Fleming, 2005; Gillum, 1995). Gender, old age, hereditary predisposition , cigarette smoking, and atherosclerotic disease are all risk factors for AAA (Lederle et al., 2000). There is no effective clinical therapy for AAA patient. Consequently, AAA grows at predictable rate. Surgery (endovascular repair and open abdominal) is known to be one of the effective forms of clinical measure for AAA cases and it is typically advised if the aneurysm is 1.9 to 2.2 inches (4.8 to 5.6 cm) in diameter or if it is expanding rapidly (Brady et al., 2004), also AAA patients must wait until their aneurysm diameter attains the surgical repair threshold, which is 4.5 cm for women and 5.5 cm for men (Brewster et al., 2003; Qin et al., 2021). The rupture threshold is defined as the moment at which the probability of rupture is predicted to outweigh the threat of surgical intervention. AAA production is assumed to be aided by elevated peripheral vascular resistance as well as adverse/proinflammatory localized hemodynamic conditions such as low and oscillatory wall shear stress. Inflammatory processes like leukocyte recruitment

mediated by elastin substances (Hance et al., 2002) and chemokines, phagocyte incursion culminating in proinflammatory cytokines and reactive oxygen compounds (Miller et al., 2002), and macrophage formation of matrix such as MMP-9 (Thompson et al., 1995) are thought to activate or encourage AAA formation and growth on a microscale.

Patients who had above-the-knee amputations , catastrophic peripheral vascular disease (Allardice et al., 1988), (Vollmar et al., 1989), and chronic trauma patients all had higher peripheral resistance compared to control groups, with rates of AAA being 2.9, 4.2, and 5.3 times higher, respectively. Last but not least, it is believed that proinflammatory/unfavorable hemodynamic circumstances like secondary flow and mild oscillatory wall shear stress promote AAA development. Through autopsy, experimental methods (Moore et al., 1994), (Tang et al., 2006) and computational techniques, it has been shown that the human aortofemoral artery, which reveals many of the same disease processes as AAAs (Boussel et al., 2008), has a connection among low or oscillatory wall shear stress and atherosclerosis. The shape of a real aneurysm, which can be fusiform or saccular, is used to determine whether it is a true aneurysm. Aneurysms with a fusiform shape are more common and are defined by the aorta expanding or inflating on all sides. Only one side of the saccular aneurysms bulges or balloons out. Aneurysm shape modifies blood flow patterns and, as a result, hemodynamic loads on the wall. From the preceding explanation, it is clear that aneurysm dilation and subsequent risk of rupture are influenced by hemodynamic loads on the wall and changes in wall mechanics, both of which are influenced by blood flow patterns. As a result, it is vital to understand better how changes in aneurysm geometry

affect blood flow patterns. Chen and Lu (Chen and Lu, 2004b) studied the newtonian and non-Newtonian rheological flow behavior was investigated in a symmetric, non-planar branching tube for steady and pulsatile blood flow (Nagargoje and Gupta, 2020; Nagargoje et al., 2021). For symmetric bifurcation, (Chaichana et al., 2012) T. Chaichana et al. analyzed flow dynamics in the left coronary artery. The angle of bifurcation ranged from 7.5 to 60 degrees. The primary vortex and areas of high shear stress have been observed to appear and vanish at the proximal and distal ends of the aneurysm bulge in both steady and pulsatile flow simulations. Additionally, axisymmetric double-aneurysm (Halabian et al., 2015) models with steady flow results show the presence of secondary solid flow behavior at the distal end. For double-aneurysm models, the oscillatory flows are dependent on the flow's Reynolds number. Viscous flow past a compliant model of arteriovenous-graft anastomosis and vein-AVG anastomosis model studied by applying the lattice Boltzmann-immersed boundary (LB-IB) framework for fluid-structure-interaction (Bai and Zhu, 2019a, 2019b). An axis-symmetric AAA model's simulations of pulsatile blood flow have demonstrated that vortices released during the preceding pulsation are pushed out and the flow reattaches close to the aneurysm wall (Joly et al., 2018; Karimi et al., 2014b; Ku and Woodruff, 1997; Rayz et al., 2008). The fact that a steady flow can precisely mimic the mean behavior patterns of its corresponding pulsatile flow has implications for flow patterns, WSS distribution, and FSS distribution. It is well known that the blood components, geometry, and mechanical strength of the arterial wall are altered by blood flow through the system; however, blood flow is dependent on the shape of the blood channel. By knowing the risk factor of AAA under various conditions like male gender, aging, cigarette smoking, and hypertension, atherosclerosis, prior surgery

(e.g., lower limb amputation), spinal cord injury genetics etc., the associated hemodynamics in AAA can be studied accordingly (Doyle et al., 2010; Humphrey and Holzapfel, 2012). People with high blood cholesterol are significantly more likely to develop aortic aneurysms than those without high cholesterol. Atherosclerosis is a condition marked by the buildup of lipids (like cholesterol) and other fatty substances on the artery walls. Typically, it affects big and medium-sized arteries. (Choudhury et al., 2019). Fat accumulation is common at the arterial bends and curved sections of the vascular arteries. Using the pressure difference seen between inner and outer walls of curved vessels (Texon, 1957), a theory linking atherosclerosis and blood flow dynamics has been proposed. The inner wall of the curve (or outer wall in the event of bifurcation) has a lower pressure than the outer wall, and the endothelium is pulled into the lumen by the transverse pressure difference throughout the channel. However, because the transverse pressure gradient is so slight that it would not generate a significant pressure change in the transverse direction, this theory was not very successful (Caro et al., 1971). Recent investigations on idealized and patient-specific vascular network models have shown that bifurcations and bending are key points of concern. Numerous bifurcations in the airflow of the respiratory system have been studied for both steady and oscillatory flow (Guha et al., 2016; Guha and Pradhan, 2017) . At bends, the mother vessel splits into two daughter blood vessels, each of which creates an angle with the mother vessel known as the bifurcation angle. Despite the fact that artery blood flow modeling has made great strides in the last decade, much of this research has relied on non-physiologic pressure and flow fields generated by boundary conditions such as zero pressure or recommended pressure or flow. The flow divides in two daughter vessels in a bifurcating vessel and flows through a curved

segment at the bifurcation. As a result, the curving influence is crucial at bifurcations as well. The flow via a curved vessel was first studied in 1902 by Williams et al.(Otero-Cacho et al., 2018), who reported a change in primary velocity toward the outer wall of curvature in their studies with water flow in a curved pipe. In a coiled pipe, Eustice (eustice, 1910) hypothesized the exsistence of secondary flow. In curved channels, Dean (R, 1911) discovered secondary flow. Soh and Berger (Soh and Berger, 1984) proposed a theory for secondary flow grounded on the balance of centrifugal force, transverse pressure gradient, and sound velocity. Raghavan et al.(Brewster et al., 2003) used finite element analysis to simulate 3-D reconstructed AAA models and discovered that the 5-cm AAA-diameter criterion was insufficient as a rupture predictor. Furthermore, prior studies primarily relied on idealized AAA shapes are simplified patient-specific models. Largely they neglected the consideration of the arteries bifurcating from the abdominal aorta such as mesenteric, renal, iliac arteries etc. Also, detailed studies on the influence of symmetric and asymmetric fusiform shape of AAA and saccular shape of AAA on the hemodynamics in the lower abdominal aortic arterial network which have significant impact on the flow entering and exiting the AAA have not been reported. Also, there has been relatively little success in applying this knowledge of hemodynamic mechanics to creating effective medical therapy for AAAs. As far as we are aware, no research has been done that examines the impact of aneurysm shape (classification of the aneurysm, bifurcation angle, neck morphology) in patient-specific aortofemoral models. Some authors mention irregular neck on blood supply in a comparative way with normal cases considering patient-specific inflow data. We have investigated the effect of realistic patient-specific abdominal aortic aneurysm shape on the hemodynamics of pulsatile Newtonian fluids. Considering all

above issue of abdominal aortic aneurysm which is not been explored yet, In this paper, we analyze hemodynamics in one normal, and four abnormal with AAA patients using magnetic resonance imaging (MRI) based DICOM data available at the open-source vascular model repository (Pfaller et al., 2022; Wilson et al., 2013) and computational fluid dynamics (CFD) technique. Computational simulations are preferred because they enable the investigation of blood flow at resolutions more precise than other medical imaging technique and can gather transient phenomena not seen by cardiac-gated imaging sequences. Also addressed in this work are the quantification of pressure and velocity, time average wall shear stress (TAWSS), oscillatory shear index (OSI), normal & critical wall shear stresses on the luminal surface of AAAs, and other hemodynamic evaluations. Patient-specific geometric models, physiologic boundary conditions, effectively resolved meshes, flow waveforms, and pressures will be used to qualitatively and quantitatively describe the reference line for the hemodynamic conditions in AAAs.

4.2 Methodology

The step by step details about methodology is described in further subsections (4.2.1-4.2.5).

4.2.1. Geometry

To study the effect of various fusiform aneurysm shape variations, i.e. (symmetric and asymmetric shape) on hemodynamics, five models of aortofemoral artery are taken, which is based on patient-specific volumetric image data available at vascular models' repository (VMR). Although actual AAA configurations differ among patients, the

three geometric parameters of interest are the aneurysm diameter (d_0), bifurcation angle θ, and aneurysms neck angle α_0 in XY Plane. (The models start from the diaphragm level and include the aorta, the hepatic and splenic arteries, the superior mesenteric artery (SMA), the right and left renal arteries, and the right and left internal and external iliac arteries. A level-set approach has been used to segment vessel borders. Each vessel's solid model is lofted separately, then combined to form a single solid model representing the flow domain as shown in (Figure 4.1). For image data orientation RAS coordinate system was assumed. The details view about all three models with dimensional details are shown in (Figure 4.2 and 4.3). The details measured dimensional values of each model (dilation diameters, neck angle, common iliac bifurcation angle, length, surface area and volume) are depicted in Tables (4.1- 4.6).

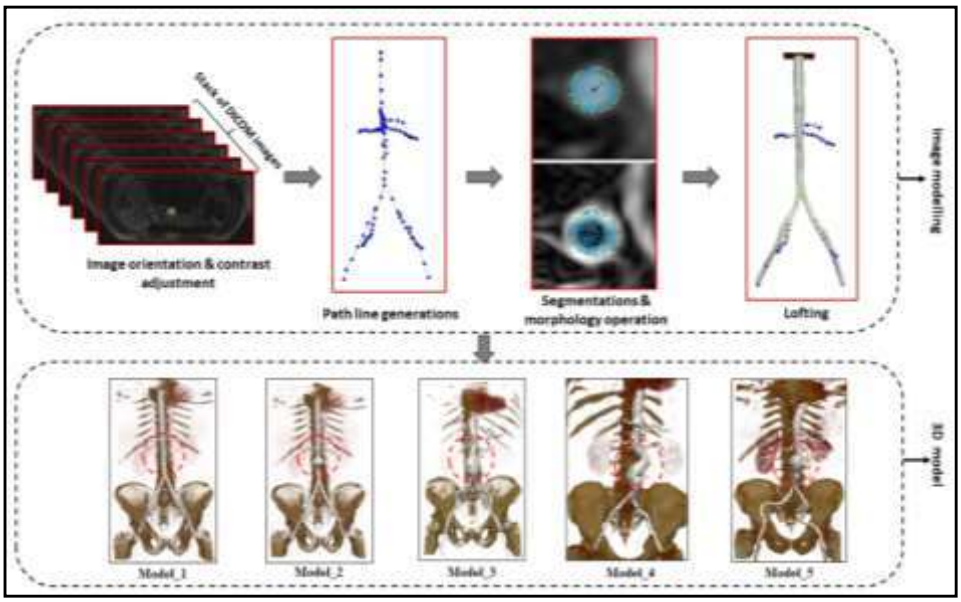

Figure 4.1 : Building a model from the MRA data (a) DICOM data, image orientation, and contrast adjustment (b) generating path lines (c) segmentation and morphology operation (d) lofting the segmentation to create blood vessel (e) unioning the vessel to generate 3d single solid model.

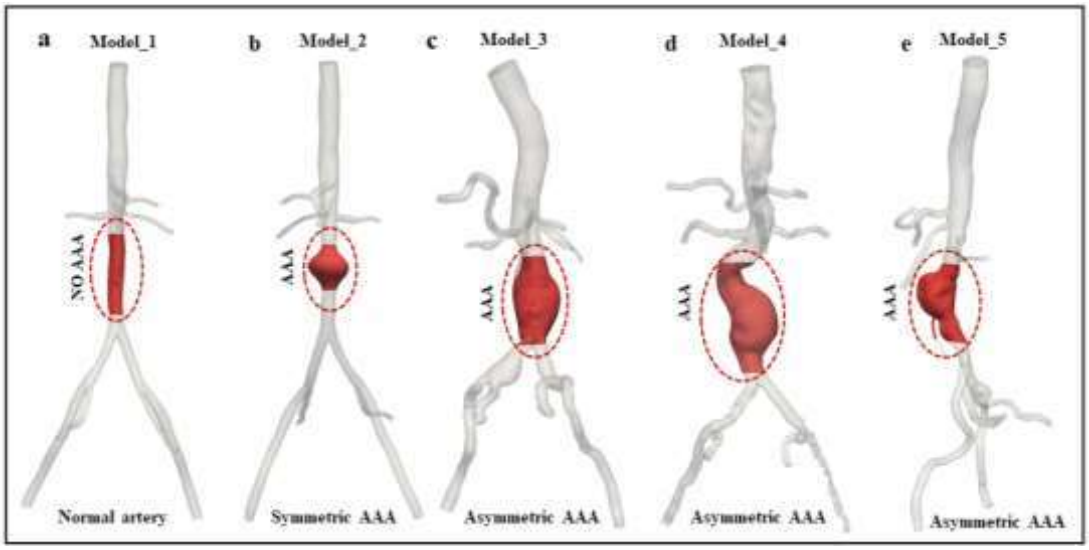

Figure 4.2 : Three-dimensional models of aortofemoral artery (a) Model_1 (b) Model_2 (c) Model_3 (d) Model_4 (e) Model_5

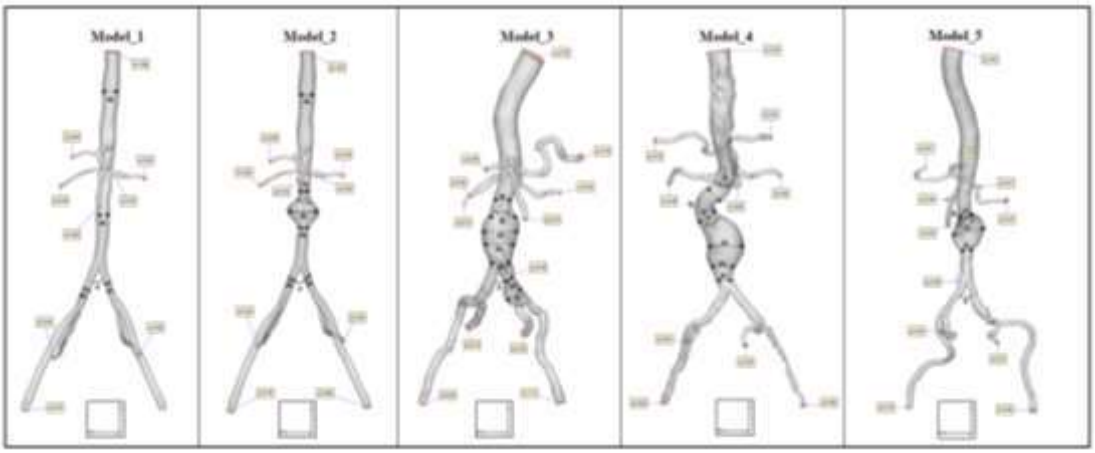

Figure 4.3 : Dimensional details of all five models (Model_1, Model_2, Model_3, Model_4, and Model_5)

Table 4.1. Geometrical parameters details of Model_1

Geometrical parameters and variations (Model_1) in XY plane						
Diamters of selected section d_0 (mm)				Bifurcation angle (θ)	Aneurysms neck angle in XY Plane (α_1)	Aneurysms neck angle in XY Plane (α_2)
d_1	d_2	d_3	d_4			
17.3	14.2	7	8	51^0	0^0	0^0

Table 4.2. Geometrical parameters details of Model_2

Geometrical parameters and variations (Model_2) in XY plane								
Diamters of selected section (mm)						Bifurcation angle (θ)	Aneurysms neck angle in XY Plane (α_1)	Aneurysms neck angle in XY Plane (α_2)
d_1	d_2	d_3	d_4	d_5	d_6			
17	11.7	32.5	11.7	8	8	47^0	33.5^0	33.5^0

TABLE 4.3. Geometrical parameters details of Model_3

Geometrical parameters and variations (Model_3) in XY plane									
Diamters of selected section (mm)							Bifurcation angle (θ)	Aneurysms neck angle in XY Plane (α_1)	Aneurysms neck angle in XY Plane (α_2)
d_1	d_2	d_3	d_4	d_5	d_6	d_7			
21	31	42	38	31	12	22	58^0	35^0	42^0

TABLE 4.4. Geometrical parameters details of Model_4

Geometrical parameters and variations (Model_4) in XY plane									
Diameters of selected section (mm)					Bifurcation angle (θ)	Aneurysms neck angle in XY Plane (α_1)	Aneurysms neck angle in XY Plane (α_2)	Aneurysms neck angle in XY Plane (α_3)	Aneurysms neck angle in XY Plane (α_4)
d_1	d_2	d_3	d_4	d_5					
17.9	21.2	35.4	20.8	15.4	65	35	41	32	39

TABLE 4.5. Geometrical parameters details of Model_5

Geometrical parameters and variations (Model_5) in XY plane					
Diameters of selected section (mm)			Bifurcation angle (θ)	Aneurysms neck angle in XY Plane (α_1)	Aneurysms neck angle in XY Plane (α_2)
d_1	d_2	d_3			
12.2	48.2	14.4	54	35	41

TABLE 4.6. All five models measured dimensional details

Normal artery geometric Model_1 details					
Number of inlets	Number of outlets	Volume(cm^3)	Surface Area(cm^2)	Number of Vessel Paths	Number of 2-D Segmentations
01	10	73.7045	281.482	09	09
Symmetric AAA geometric Model_2 details					
Number of inlets	Number of outlets	Volume(cm^3)	Surface Area(cm^2)	Number of Vessel Paths	Number of 2-D Segmentations
01	10	86.0479	298.019	09	09
Asymmetric AAA geometric Model_3 details					
Number of inlets	Number of outlets	Volume(cm^3)	Surface Area(cm^2)	Number of Vessel Paths	Number of 2-D Segmentations
01	11	219.061	510.317	11	11
Asymmetric AAA geometric Model_4 details					
Number of inlets	Number of outlets	Volume(cm^3)	Surface Area(cm^2)	Number of Vessel Paths	Number of 2-D Segmentations
01	09	129.0955	350.2656	09	09
Asymmetric AAA geometric Model_5 details					
Number of inlets	Number of outlets	Volume(cm^3)	Surface Area(cm^2)	Number of Vessel Paths	Number of 2-D Segmentations
01	10	166.0742	440.4181	10	10

4.2.2 Discretization

To study the numerical solution of blood flow using partial differential equations, discretization is necessary. The model was discretized into an initial isotropic finite-element mesh with a maximum global max edge size of 0.0798 mm using the finite element meshing module called svSolver under SimVascular. For boundary layer meshing portion of edge size is 0.50, number of layers is 3 and layer decreasing ratio is 0.80. The details about the mesh parameter are described in the Table 4.7. To do mesh validation fine (0.0798 mm), coarse (0.1562 mm) and medium (0.0998 mm) type mesh parameter is considered and their validation are checked as shown in (Figure 4.4). Mesh validation and independency check using plot of WSS with respect to cardiac cycle by considering three local points on the wall of the Model_1 is also described in (Figure 4.5).

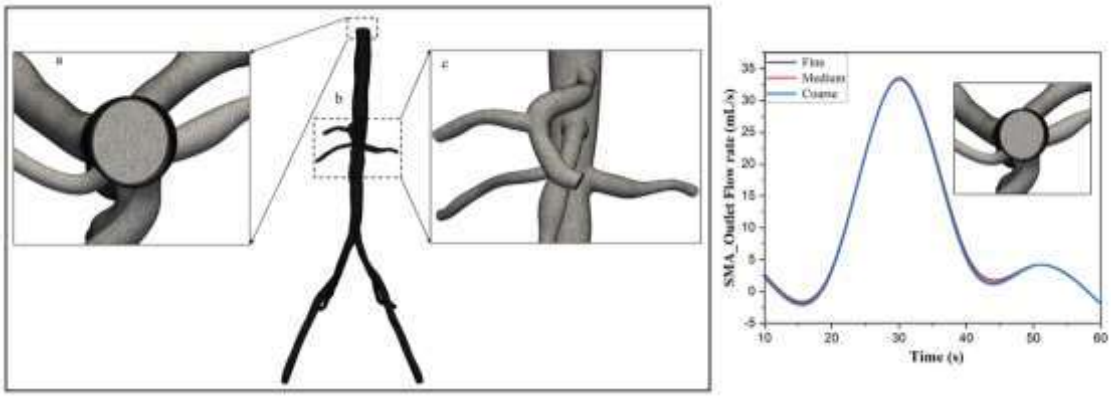

Figure 4.4: 3D mesh view of Model_1 and with mesh independency check; (a) magnified view of mesh showing inflation layers at the inlet (b) 3D mesh Model_1 (c) magnified view of mesh in the middle of the Model_1 and right-side graph shows mesh validation using flow rate waveform at SMA outlet with respect to cardiac cycle considering fine, medium and coarse mesh sizes.

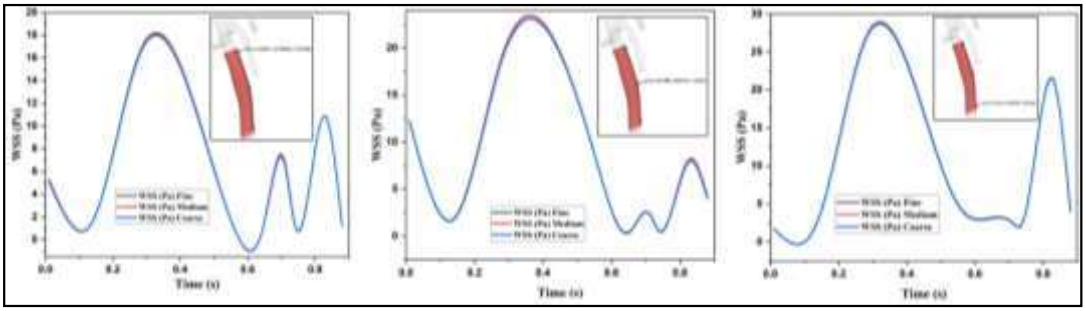

Figure 4.5 : Mesh validation and independency check using WSS versus time at different spatial locations on the normal Model_1 artery given by the (x, y, z) coordinates in mm. WSS is shown at the selected region of interest (red colour) i.e., at the middle of the abdominal artery. The coordinates of three points taken on the superior, middle and inferior location of the wall are: P_1 (-1.62607, 2.678528, 1.732188), P_2 (-1.437388, 3.846733, -1.6169) and P3 (-1.132112, 4.305058, -5.96346).

TABLE 4.7. Mesh details of all five models of aortofemoral arteries

Models	Mesh Details	
	Number of cells	Number of points
Model_1	3573998	660349
Model_2	2657891	459029
Model_3	2937020	548038
Model_4	2983028	550959
Model_5	3321382	625163

4.2.3. Governing equations

The Navier–Stokes and continuity equations, which describe the conservation of momentum and mass of a Newtonian incompressible fluid, are used to model blood flow in an arbitrary numerical domain Ω with boundary Γ. The boundary Γ is set in such a way that $\Gamma = \Gamma_i \cup \Gamma_w \cup \Gamma_h$; $\Gamma_i \cap \Gamma_w \cap \Gamma_h = \emptyset$, where Γ_i represent an inlet boundary where the velocity field is subjected to a Dirichlet condition; Γ_w indicates the vessel's outer wall; and Γ_h depicts all the outflow

boundaries where a Neumann constraint is imposed. The aforementioned partial differential equations, when applied to the suitable boundary and initial conditions, define a well-posed Initial Boundary Value Problem viz.:

$$\left.\begin{aligned} \rho\vec{u}_t + \rho\vec{u}\cdot\nabla\vec{u} &= -\nabla p + div\left(\underset{\sim}{\tau}\right) + \vec{f} \\ div(\vec{u}) &= 0 \\ \underset{\sim}{\tau} &= 2\,\mu\underset{\sim}{D} \quad \text{with} \quad \underset{\sim}{D} = \frac{1}{2}\,(\nabla\vec{u} + \nabla\vec{u}^{\,T}) \end{aligned}\right\} \quad \text{in } \Omega \qquad (1)$$

$$\vec{u}\,(\vec{x},t) = \vec{u}^{\,in}(x,t) \qquad \vec{x} \in \Gamma_i \qquad (2)$$

$$\vec{u}\,(\vec{x},t) = \vec{0} \qquad \vec{x} \in \Gamma_w \qquad (3)$$

$$\vec{t}_{\vec{n}}\,(\vec{x},t) = \left[-p\underset{\sim}{I} + \underset{\sim}{\tau}\right].\vec{n} = \vec{h}\,(\vec{x},t) \qquad \vec{x} \in \boldsymbol{\Gamma}_h \qquad (4)$$

$$\vec{u}\,(\vec{x},0) = \vec{u}^0(\vec{x}) \qquad \vec{x} \in \Omega \qquad (5)$$

The blood velocity $\vec{u} = (u_x, u_y, u_z)$ and the pressure *p* are the main variables here. The density ρ and viscosity μ of the blood is assumed to be constant (ρ = 1.06 g/cm^3, μ = 0.04 P). As shown in Eq. (3), the external body force *f* representing gravity is omitted, and the vessel wall boundary is considered to be rigid. Please notice that $\vec{h}$ in Eq. (4) represents the traction vector imposed on the outflow boundaries Γ_h. We used the following trial solution and weighting function spaces to define the variational form corresponding to Eqs. (1)-(5):

$$S = \left\{\vec{u} \middle| \vec{u}(.,t) \in H^1(\Omega)^{n_{sd}}, t \in [0,T],\ \vec{u}(.,t) = \vec{u}^{in} \text{ on } \Gamma_i,\ u(.,t) = \vec{0} \text{ on } \Gamma_w \right\}$$

$$W = \left\{\vec{w} \middle| \vec{w}(.,t) \in H^1(\Omega)^{n_{sd}}, t \in [0,T],\ \vec{w}(.,t) = \vec{0} \text{ on } \Gamma_i,\ w(.,t) = \vec{0} \text{ on } \Gamma_w \right\}$$

$$P = \{p \mid p(.,t) \in H^1(\Omega), t \in [0,T]\} \quad (6)$$

$H^1(\Omega)$ represents the space of all square-integrable functions whose and first derivatives are also square-integrable in Ω and n_{sd} is the number of spatial dimensions. As a result, the variational formulation for this situation is as follows:

$$B_G(\vec{w}, q; \vec{u}, p) = 0$$

$$B_G(\vec{w}, q; \vec{u}, p) = \int_\Omega \left\{\vec{w}.\left(\rho\vec{u}_{,t} + \rho\vec{u}.\nabla\vec{u} - \vec{f}\right) + \nabla\vec{w} : \left(-p\underset{\sim}{I} + \underset{\sim}{\tau}\right)\right\}\overrightarrow{dx} -$$

$$\int_\Omega \nabla q.\vec{u}\, d\vec{x} - \int_{\Gamma_h} \vec{w}.\left(-p\underset{\sim}{I} + \underset{\sim}{\tau}\right).\vec{n}ds + \int_\Gamma q\vec{u}.\vec{n}ds \quad (7)$$

Vignon-Clementel et al.(Vignon-Clementel et al., 2006) proposed a Coupled-Multidomain formulation, which we used. Please note that $\vec{w} \in W$ and $q \in P$.This method is based on a variational multiscale decomposition of the domain Ω into an upstream 3D numerical domain $\widehat{\Omega}$ and a downstream reduced-order analytical domain Ω' where $\widehat{\Omega} \cap \Omega' = \emptyset$ and $\overline{\widehat{\Omega} \cup \Omega'} = \Omega$. An interface called Γ_B Separates the numerical and analytical domains. Throughout this work, we will refer to this interface as an "outlet" or "outlets" (of the 3D computational domain). The approach also takes into account a disjoint decomposition of the flow variables: the solution vector $\vec{V} =$

$\{\vec{u}, p\}^T$ is divided into two components, one defined in the numerical region and the other in the analytical domain, viz.

$$\vec{V} = \left\{\hat{\vec{V}} + \vec{V}'\right\} \text{ with } \hat{\vec{V}}\Big|_{\Omega'} = 0 \text{ and } \vec{V}'\Big|_{\hat{\Omega}} = 0 \qquad (8)$$

This decomposition satisfies $\hat{\vec{V}} = \vec{V}'$ at the interface Γ_B, and is also implemented to the weighting functions $\vec{w}$ and q. Under these assumptions, Eq. (7) can be rewritten as:

$$\int_{\hat{\Omega}} \hat{\vec{w}} \cdot \left(\rho \hat{\vec{u}}_{,t} + \rho \hat{\vec{u}} \cdot \nabla \hat{\vec{u}} - \hat{f}\right) + \nabla \hat{\vec{w}} : \left(-\hat{p} \underset{\sim}{I} + \underset{\sim}{\hat{\tau}}\right) d\vec{x} - \int_{\hat{\Gamma}_h} \hat{\vec{w}} \cdot \left(-\hat{p} \underset{\sim}{I} + \underset{\sim}{\hat{\tau}}\right) \cdot \vec{n} ds +$$

$$\int_{\Gamma_B} \vec{w}' \cdot \left(-p' \underset{\sim}{I} + \underset{\sim}{\tau'}\right) \cdot \vec{n}' ds - \int_{\Omega} \nabla \hat{q} \cdot \hat{\vec{u}} d\hat{x} + \int_{\hat{\Gamma}} \hat{q} \hat{\vec{u}} \cdot \hat{\vec{n}} ds - \int_{\Gamma_B} q' \vec{u}' \cdot \vec{n}' ds = 0$$

(9)

At the interface between the numerical and analytical domains, the integral terms defined on Γ_B represent the continuity of traction and flow. These terms can be approximated by the operators.

$\boldsymbol{M} = \left\{M_m, \vec{M}_c\right\}\Big|_{\Gamma_B}$ and $\boldsymbol{H} = \left\{H_m, \vec{H}_c\right\}\Big|_{\Gamma_B}$:

$$\int_{\Gamma_B} \vec{w}' \cdot \left(-p' \underset{\sim}{I} + \underset{\sim}{\tau'}\right) \cdot \vec{n}' ds - \int_{\Gamma_B} q' \vec{u}' \cdot \vec{n}' ds \approx \int_{\Gamma_B} \vec{w}' \cdot \left(\underset{\sim}{M}_m (\vec{u}', p') + \underset{\sim}{H}_m\right) \cdot \vec{n}' ds - \int_{\Gamma_B} q' \left(\vec{M}_c (\vec{u}', p') + \vec{H}_c\right) \cdot \vec{n}' ds \qquad (10)$$

The operators **M** and **H** are well-defined in the domain Ω' based on the reduced-order model chosen to denote flow and pressure in the downstream domain (i.e., morphometry-based impedance function, lumped parameter model, etc.) as shown in (Figure 4.6) The final weak form of the Coupled-Multidomain method fallouts in (Vignon-Clementel et al., 2006).

$$\int_{\widehat{\Omega}} \widehat{\vec{w}} \cdot \left(\rho \hat{\vec{u}}_{,t} + \rho \hat{\vec{u}} \cdot \nabla \hat{\vec{u}} - \hat{f}\right) + \nabla \widehat{\vec{w}} : \left(-\hat{p} \underset{\sim}{I} + \underset{\sim}{\hat{\tau}}\right) d\vec{x} - \int_{\widehat{\Gamma}_h} \widehat{\vec{w}} \cdot \left(-\hat{p} \underset{\sim}{I} + \underset{\sim}{\hat{\tau}}\right) \cdot \hat{\vec{n}} ds - \int_{\Gamma_B} \vec{w}' \cdot \left(\underset{\sim}{M}_m (\hat{\vec{u}}, \hat{p}) + \underset{\sim}{H}_m\right) \cdot \hat{\vec{n}} ds - \int_{\widehat{\Omega}} \nabla \hat{q} \cdot \hat{\vec{u}} d\vec{x} + \int_{\Gamma} \hat{q} \, \hat{\vec{u}} \cdot \hat{\vec{n}} ds + \int_{\Gamma_B} \hat{q} \cdot \left(\overrightarrow{M_c} (\hat{\vec{u}}, \hat{p}) + \vec{H}_c\right) \cdot \hat{\vec{n}} ds = 0 \qquad (11)$$

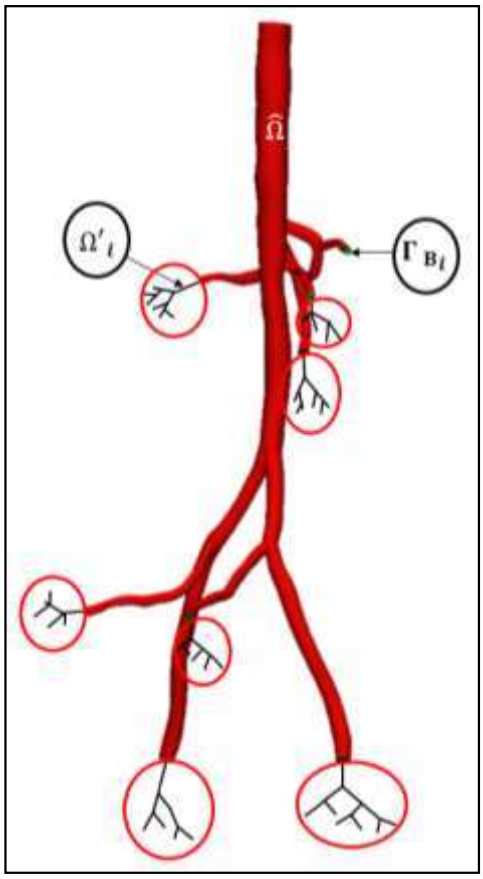

Figure 4.6 : The spatial domain is divided between the upstream numerical domain $\widehat{\Omega}$ (main model) and the downstream analytic domain $\widehat{\Omega} = \cup_i \ \widehat{\Omega}'_i$ (here the trees), separated by the coupling boundary $\Gamma_B = \cup_i \Gamma_{B_i}$ (here in green).

Note that the solution in the numerical domain $\widehat{\Omega}$ depends on the operators demarcated by the mathematical model chosen for the downstream analytical domain, stated as a function of the solution variables of the numerical domain $\{\hat{\vec{u}}, \hat{p}\}$. For a three-element

Windkessel (R_p, C, R_d) model of the downstream vasculature, the operators **M** and **H** become (Vignon-Clementel et al., 2010)

$$\underset{\sim}{M}_m\left(\hat{\vec{u}},\hat{p}\right) = R_p \int_{\Gamma_B} \hat{\vec{u}}\,.\,\hat{\vec{n}}ds + \int_0^1 \frac{e^{-(t-t_1)/\tau}}{C} \int_{\Gamma_B} \hat{\vec{u}}\,(t_1)\,.\,\hat{\vec{n}}dsdt_1 + \hat{\vec{n}}.\,\underset{\sim}{\hat{\tau}}\,.\,\hat{\vec{n}} - \underset{\sim}{\hat{\tau}}$$

$$\underset{\sim}{H}_m = \left(\hat{P}(0) - R_p \int_{\Gamma_B} \hat{\vec{u}}\,(0).\,\hat{\vec{n}}d\Gamma - \hat{P}_d(0)\right)e^{-t/\tau} + \hat{P}_d(t)$$

$$\vec{M}_c\left(\hat{\vec{u}}\,.\hat{p}\right) = \hat{\vec{u}}$$

$$\vec{H}_c = \vec{0} \qquad (12)$$

where $\tau = \mathrm{R}_d C$. Here, R_p denotes the proximal resistance, C is the capacitance, and R_d is the distal resistance of the downstream vasculature; P_d is a time-varying function representing the terminal capillary pressure. *P(0), Q(0), and P_d (0)* are the initial conditions for pressure, flow, and capillary pressure for the downstream analytical domain, respectively.

The boundary and initial conditions (2)-(5), as well as the variational form defined by Eqs. (11) and (12), are then solved using a novel stabilized finite-element solver that uses equal-order interpolation for velocity and pressure (Steele et al., 2007; Vignon-Clementel et al., 2010; Whiting and Jansen, 2001) All simulations were carried out using direct numerical simulations, with no assumptions about the flow being laminar or fully developed turbulent. This is justified because most turbulence models assume fully developed turbulent conditions, which is not the case for pulsatile flow in AAAs. The flow, undoubtedly turbulent during late systole, largely relaminarizes during early systole and diastole (Taylor and Steinman, 2010).

4.2.4 Simulation setup

The modeling for a single patient is described below. The simulation process described here is repeated for all the patient data in a patient-specific way. Simulations have been performed for eight cardiac cycles , where the number of time steps is 250 and time step size 0.04 , with three nonlinear iterations per time step have been defined in order to ensure uniformity in results. At the wall, a no-slip condition was prescribed, as indicated in Eq. (3). A patient specific inflow waveform derived from PC-MRI data available from simvascular repositry has been prescribed to the inlet of the computational fluid dynamics (CFD) model and individually inflow waveform are applied to all five models in this study. In the simvascular solver (svLS) for solving navier stokes (NS) flow problems , we have incorporated implicit pressure coupling method and the tolerance of 10^{-3} for solution convergence. A three-element Windkessel model with proximal resistance (R_p), capacitance (C), and distal resistance (R_d) are used for downstream of each outlet to depict the resistance and capacitance of the proximal vessels (the arteries), as well as the resistance of the distal vessels (the arterioles and capillaries) (Figure 4.7). Here we prescribe patient specific flow wave via a dirichlet condition on the velocity vectors of the inlet which contain information about fluid density, fluid viscosity, velocity profile shape, period length, number of points in one period, number of fourier modes, inlet face, and flow file . By using this condition here, we are making the face outlet into a weakly-pressure face. This is mathematically expressed by the expressions we saw before:

$$p = p_0 + RQ$$

$$p(t) = p_0 + \frac{1}{T} \int_{t-T}^{t} Z\,(t-\tau)Q(\tau)\,d\tau \qquad (13)$$

This expression sets $p_0 = 0$ for the face outlet pressure. where Q & R is the localize volumetric flow rate and resistance. The total pressure set on that face will be the result of the flow-pressure operator considered in RCR lumped parameters condition. Here spatially-constant pressure boundary condition is weakly enforced via a resistance R. The tune RCR values for each five models based on the inflow rate of each patient are described in Table. 4.8.

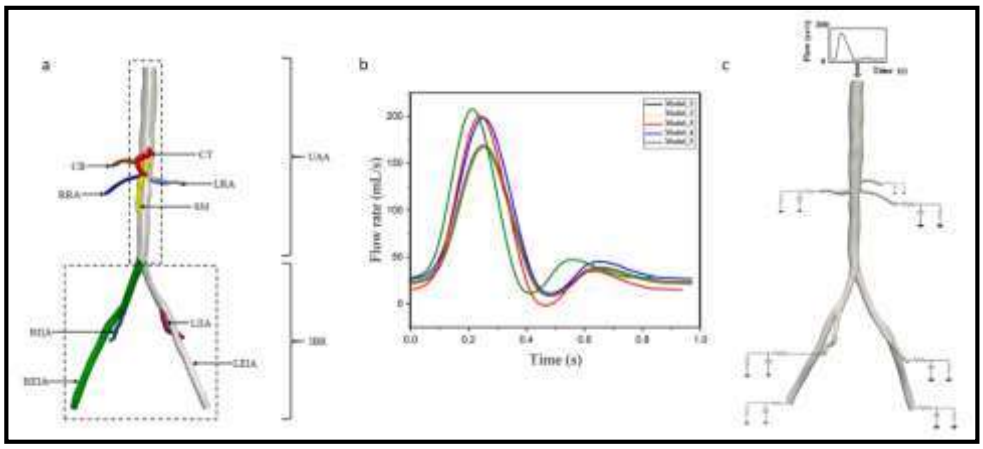

Figure 4.7 : A patient-specific flow waveform measured by phase-contrast MRI (resting conditions) from an opensource vascular repository is imposed to the inlet face using a Womersley velocity profile. (a) Shows 3d Model_1 with anatomical details in which the outlet labels are as follows: CB= celiac branch, CT=celiac trunk, RRA= right renal artery, LRA=left renal artery, SM= superior mesenteric, LIIA= left internal iliac artery, RIIA=right internal iliac artery, LEIA= left external iliac artery, REIA= right external iliac artery. (b) Inflow waveforms for all five models (c) Shows a patient-specific 3-element Windkessel model with a proximal resistance (R_p), capacitance (C), and distal resistance (R_d) boundary condition is used to represent the resistance and compliance of the vasculature downstream of each outlet.

TABLE 4.8. Calculated R_p, C, R_d Specification for all three models

RCR Values for Each Outlet (Model_1)			RCR Values for Each Outlet (Model_2)			RCR Values for Each Outlet (Model_3)			RCR Values for Each Outlet (Model_4)			RCR Values for Each Outlet (Model_5)		
Face Name	R_{p1}	C_1	R_{d1}	R_{p2}	C_2	R_{d2}	R_{p3}	C_3	R_{d3}	R_{p4}	C_4	R_{d4}	R_{p5}	C_5	R_{d5}
REIA	1552.3884	0.000433917	19810.34334	1552.3884	0.000433917	19810.34334	2086.615	8.81E-05	20495.92	1408.465469	0.00010223	13781.98229	949.065543	0.000139643	21345.9452
LEIA	1552.38326	0.000433917	19787.59127	1552.38326	0.000433917	19787.59127	2086.615	8.81E-05	20495.92	1250.169729	0.00010223	17016.14677	949.837506	0.000139643	21369.94741
HA	1493.57453	0.000450977	18269.67796	1493.57453	0.000450977	18269.67796	2472.554	7.44E-05	23853.67	1163.888045	0.00011045	15344.32222	644.270695	0.000205037	14050.82467
SA	1493.631	0.000450977	18709.24499	1493.631	0.000450977	18709.24499	1162.789	0.000158	11295.36	1138.974315	0.00011541	14645.50005	813.334855	0.000163	17289.21583
SMA	1101.49575	0.000611524	13829.80209	1101.49575	0.000611524	13829.80209	1167.634	0.000157	11393.54	842.278647	0.00015736	11484.45912	527.867174	0.000249608	11415.72845
RRA	958.80215	0.000702475	11009.01237	958.80215	0.000702475	11009.01237	970.3029	0.000189	8783.22	712.164878	0.00018202	9066.420888	505.085306	0.000299724	8114.201674
LRA	958.81242	0.000702475	11248.95255	958.81242	0.000702475	11248.95255	970.7677	0.000189	8998.073	706.680702	0.00018202	9105.820592	686.752984	0.000299724	6954.844667
RIIA	3622.20536	0.000185963	46011.16506	3622.20536	0.000185963	46011.16506	4871.868	3.78E-05	47906.82	2928.703415	4.38131e-05	39559.16171	2212.328515	5.98471e-05	49812.0729
LIIA	3622.20023	0.000185963	45957.94308	3622.20023	0.000185963	45957.94308	4871.868	3.78E-05	47906.82	2919.10641	4.38131e-05	39718.05348	2219.931507	5.98471e-05	50088.08254

4.2.5 Hemodynamic paramter calculation

4.2.5.1 Time average wall shear Stress (TAWSS)

To assess the wall shear stress acting on the lumen wall under pulsating flow in aortofemoral circulation, in normal and diseased cases, Time Average Wall Shear Stress (TAWSS) and Oscillatory Shear Index (OSI) can be used.

$$TAWSS = \frac{1}{T} \int_0^T |WSS| \, dt \quad \text{..... (14)}$$

Where T is the period of the cardiac cycle, and WSS is the WSS vector.

4.2.5.2 Oscillatory shear index (OSI)

To evaluate axial directional change in WSS within the cardiac cycle Oscillatory Shear Index (OSI) are a frequently used index. OSI is an essential measure of hemodynamic forces acting on the wall, but unfortunately, is not often reported in the literature. Several studies have reported highly oscillatory flow within AAAs, but include small sample sizes, or fail to report average values within the AAA and the proximal or distal aorta. Also, abnormal OSI shows that the flow field is highly disturbed, associated with the formation of thrombosis (Xiang et al., 2014). OSI is defined as follows:

$$OSI = 0.5 \times \left[1 - \frac{\left|\int_0^T WSS dt\right|}{\int_0^T |WSS| dt}\right] \quad \text{.....(15)}$$

Where T is the cardiac cycle period, and WSS is the WSS vector.

4.2.5.3 Vortex structures

The vortex structures are an important flow parameter in the aneurysms and can be represented by the Q-criterion (JEong and Hussain, 1995; Jiang et al., 2005)(Nagargoje et al., 2022) .The Q-criteria can be calculated from the velocity gradient tensor and can be written as follows:

$$\nabla\vec{u} = S + \Omega \quad (16)$$

Where $S = \frac{1}{2}\left[(\nabla\vec{u}) + (\nabla\vec{u})^T\right]$ is the rate of strain tensor, and $\Omega = \frac{1}{2}\left[(\nabla\vec{u}) - (\nabla\vec{u})^T\right]$ is a vorticity tensor.

Hunt et al. (Nagargoje et al., 2022) defined a vortex as a spatial region where $S = \frac{1}{2}[|\Omega|^2 - |S|^2] > 0$ (17)

4.3 Results and discussion

Five patient-specific models of aortofemoral arteries have been considered to investigate the aneurysm shape effect on hemodynamics. The five models are categorized according to their aneurysms shape and location, i.e., Model_1 (normal vessel), Model_2 (symmetric infrarenal), Model_3 (asymmetric fusiform), Model_4 (asymmetric infrarenal) and Model_5 (asymmetric saccular). All five models are numerically solved using an open-source finite element solver, i.e., simVascular for computational fluid dynamics (CFD) studies. The simulations performed in order to evaluate the hemodynamics parameters like velocity distribution, flow patterns, wall shear stress, oscillatory shear index, and vorticity in the localized region of interest of

all five models. The unsteady flow simulations run for ten cardiac cycles to reduce the impact of initial transients.

The cardiac flow cycle is divided into two stages. The first phase, during which the flow accelerates, is referred to as the systolic phase, while the second phase, during which the flow decelerates, is referred to as the diastolic phase. (Figure 4.8) depicts the computational domain with spatial location and their medical nomenclature. The results are displayed at various necessary time intervals to explain the transient blood flow dynamics:

T_0 = 0.01 is the start of systolic phase

T_1 = 0.14 is the acceleration of the systolic phase

T_2 = 0.28 is the peak of the systolic phase

T_3 = 0.56 end of the systolic phase

T_4 = 0.65 is the start of the diastolic phase

T_5 = 0.71 is the start of the diastolic phase

T_6 = 0.74 is the peak of the diastolic phase

T_7 = 0.83 is the deceleration of the diastolic phase

T_8 = 0.88 is the end of the diastolic phase

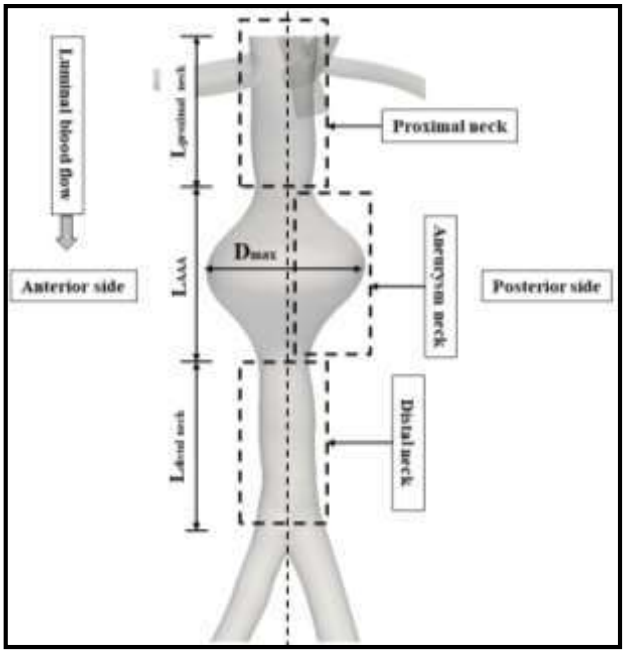

Figure 4.8 : Computational domain and geometrical parameters used for AAA hemodynamics evaluation

The parametric factors influencing the nature of blood flow within an aneurysm are aneurysm sac diameter, shape, and parent artery diameter. The amount of flow entering the aneurysm sac is determined by the neck size, and the volume of the aneurysm determines how slow the flow is in the aneurysm sac. In the further subsection of the results, the effect of aneurysm shape, bifurcation angles, and patient-specific pulsatile inflow conditions are investigated.

4.3.1 Effect of aneurysms vessels dilation on velocity distributions

(Figure 4.9) depicts the effect of aneurysm dilation on velocity distribution on the horizontal cross-sectional view of all four diseased models at T_3, T_5, and T_6 instant of the cardiac cycle. As shown in (Figure 4.9) six horizontal cross-sectional slides (S1-S6) from the start to the end of aneurysms in all four pathological models are considered for velocity distribution. The velocity contours within the horizontal cross-

sectional slides reveal that the magnitude of velocity changes significantly over time and space. From Figure 4.3.1in Model_2, which is an infrarenal symmetric aneurysm, it is observed that during T_3 at section S1, the velocity is fully developed; however, its magnitude falls due to enlargement of central diameter, and at the distal of aneurysms the velocity distribution spatially changes, however during T_5 and at S3 the velocity is maximum at the midsection of the symmetric aneurysms and significant differences is noted in velocity magnitude during T_3, T_5, and T_6 as seen from the corresponding axial velocity waveform of the section S3. In Model_3, as shown in (Figure 4.9), which is asymmetric fusiform aneurysms, it is noted that the velocity is maximum at the proximal section of the aneurysm and changes spatially with the effect of dilation of the blood vessel, during T_3 and at S3 cross-section the velocity is maximum in the distal inner wall of the slice. However, during the diastolic phase, the velocity magnitude decreases at T_5 and T_6 with the nonlinear waveform, as seen in the corresponding waveform of the axial velocity. Also, the recirculation zone is noted due to asymmetric bulging of the blood vessel and diastolic phase near the inner wall of the cross sections S3, S4, and S6. In model_4, which is an asymmetric infrarenal aneurysm, it is found that during T_3, the velocity is fully developed at the start of the aneurysm, i.e., on cross-section S1, a secondary motion started near the inner wall of the cross section S3 in an anterior position which starts forming recirculation zone, and similar trend of velocity distribution is noted on sections S1, S3 and S6 during T_3 and T_5 with slightly less in magnitude as shown in corresponding axial velocity waveforms in (Figure 4.9) also, due to double tilting of the aneurysm neck angle and diastolic velocity pulse during T_6, the velocity distribution abruptly changes on sections S1, S3, and S6 as seen in Figure 4.3.1In Model_5, which is an asymmetric infrarenal saccular aneurysm which is having

a high risk of rupture due to its shape, it is noted that on section S1, at T_3, the velocity is maximum near the inner wall of the inferior location and due to saccular shape double recirculation zone start forming which reduces the blood flow in the toe region of the aneurysms as seen in the figure at section S6. Also, it is noted that during T_6, which is the end of diastole on section S3 the velocity starts forming a circular shape in the anterior inner wall of the cross-section, and at section S6, the velocity again attends fully developed, and it can be seen from corresponding axial velocity waveforms that trend line is quite similar on section S3 and S6, but variation in their magnitude is noted which may affect the other blood flow in the downward regions. It is noted from all models that the effect of aneurysm dilatation alters the flow velocity distribution, which may influence the lower extremities' blood circulation.

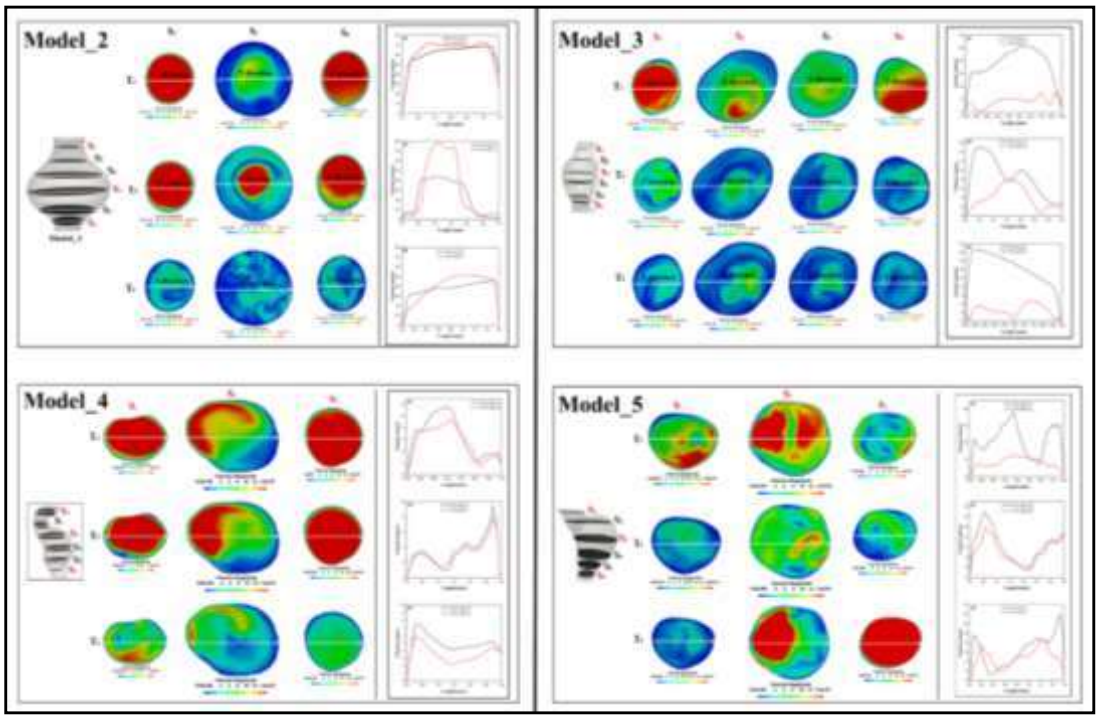

Figure 4.9 : Blood flow velocity distribution over the cross sections at the top, mid, and toe of the aneurysm and corresponding axial velocity waveform at peak systole T_3 and peak diastole T_5

4.3.2 Effect of the neck angle and aneurysm's location on the velocity distribution

(Figure 4.10) demonstrates the effect of the aneurysm's neck angle and its location on velocity distribution with vectors in the longitudinal cross-section view of all four models from the start of the neck angle to the start of the iliac bifurcation. In Model_2, having a symmetric neck angle i.e. $\alpha_1 = 33.5^0$, $\alpha_2 = 33.5^{0,}$ it is noted that from the start of the systolic phase, two large vortices forms near the distal end in the symmetric view shown with an arrow on both sides of infrarenal aneurysms during the peak of the systolic phase at T_2 flow is maximum in the core region of the longitudinal slice and at T_7 it attains the same pattern but slightly lesser in magnitude because of diastolic phase. Because of two vortices formation during the accelerating and decelerating phase of the systolic and diastolic phase it leads to platelet deposition and thrombus formation leading to the weakening of the wall and increasing the chance of rupture at the aneurysm's sac location. In Model_3, which is an asymmetric fusiform aneurysm having neck angle, $\alpha_1 = 35^0$, $\alpha_2 = 42^0$ it is noted that with a change in neck angle due to asymmetric dilation of the blood vessel in the systolic phase, vortex formation started from head to toe of the aneurysm, however the spatial location of vortex changes during the diastolic phase of the cardiac cycle. Also, lower velocity and recirculation are present in the aneurysmal sac region. It has been identified that there is a main flow channel that originates in the neck region of the aneurysm and is characterized by higher velocities during T_2, T_3, and T_4. However, due to the influence of asymmetric dilation in fusiform aneurysms, the velocity magnitude drops and secondary flow begins to form. In the Model_4, which is asymmetric infrarenal doubly twisted in the

shape of an aneurysm having neck angle $\alpha_1 = 35^0$, $\alpha_2 = 41^0$, $\alpha_3 = 32^0$, $\alpha_4 = 39^0$, it is noted that velocity is maximum and fully developed during T_3 and T_8 which is because of the doubly twisting aneurysm shape. Also, during T_4 two vortexes formed at the start of the cross-section and mid of the aneurysm. In Model_5 is asymmetric saccular aneurysm in shape with a neck angle $\alpha_1 = 35^0$, $\alpha_2 = 41^0$ it is noted that during T_0, T_2, T_4, T_6, and T_8 the fully developed velocity is formed from the neck to the distal end of the saccular aneurysm. Also, it is noted that flow separation occurs during systolic deceleration, and the vortex begins to travel in the aneurysm sac. Due to the saccular in the shape of an aneurysm, many vortexes start forming in the distal end of the aneurysm, which can create thrombosis formation leading to rupture.

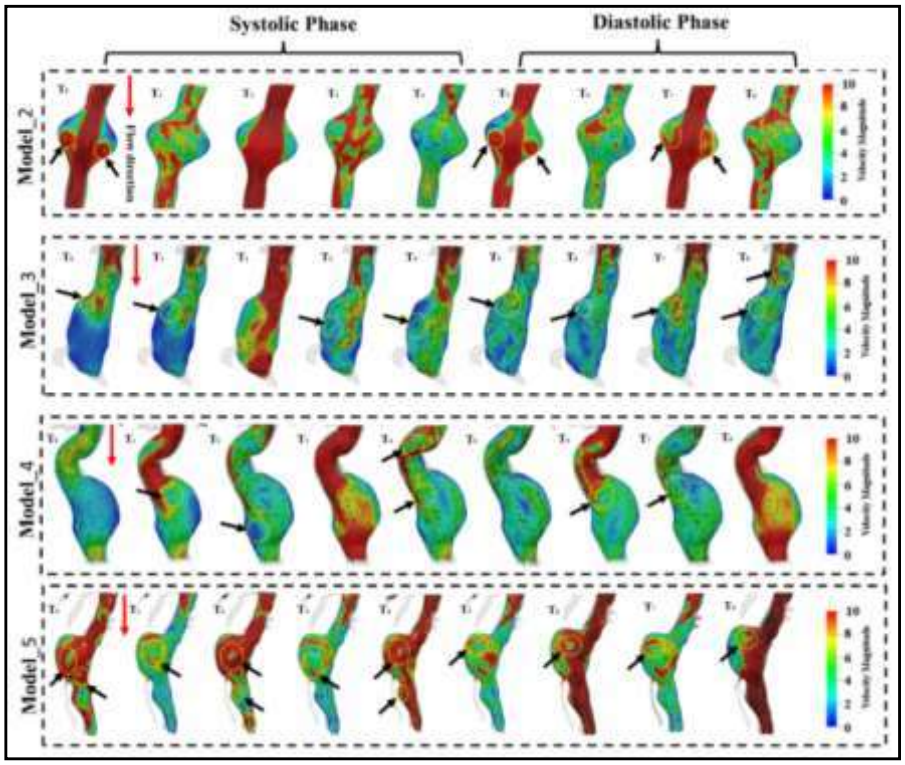

Figure 4.10 : Effect of neck angle on velocity distribution in the longitudinal cross-section from start of neck angle to start of iliac bifurcation in all four models at various instant of cardiac cycle (T_0-T_8).

4.3.3 Effect of neck angle and aneurysm's location on flowlines

(Figure 4.11) depicts the streamlines of the blood flow in the three-dimensional view from the start of the neck angle to the distal end of the aneurysms in all four models of aneurysms in artofemoral arteries. In Model_2, which is a symmetric aneurysm having neck angle $\alpha_{1,2} = 33.5^0$, it is seen from the blood flow lines that during the start of the systolic phase, two vortices formed on both side of the distal end of the aneurysm however, with the acceleration of the systolic phase, the flow lines start getting irregular in the pattern at T_1 , at T_2 maximum in magnitude with uniform lines near central core region, while during deceleration of systolic phase recirculation start forming and during diastolic phase at T_7 again large vortices formed in the symmetric pattern. Also, during peak systole i.e., at T_2 the flow lines are almost regular in pattern; however, during peak diastole i.e., at T_7 the flow lines are regular in pattern from head to toe of aneurysms but with large vortices formed in the mid-region of the bulging portion. The Model_3, which is fusiform asymmetric in shape, has neck angle $\alpha_1 = 35^0$, $\alpha_2 = 42^0$, it is noted that because of different neck angle at the start of aneurysm the flow lines near the proximal head of aneurysm are regular in shape at the peak of systole, i.e., T_2 and peak diastole T_7; however, flow lines gets irregular with deceleration, of peak systole and diastole phase. Also, many irregularities in flow lines and small vortices near the proximal head of the aneurysm are seen from the mid to distal end of the aneurysms as shown in (Figure 4.11) with dotted box . In Model_4, which is doubly tilted in aneurysm shape having a neck angle $\alpha_1 = 35^0$, $\alpha_2 = 41^0$, $\alpha_3 = 32^0$, $\alpha_4 = 39^0$, it has been seen that from early systole, i.e., from T_0 to flow lines, gets separated from the start of the neck of first tilting, and with velocity acceleration

stagnation, vortex formation and intensification and shedding in flow lines are noted in the sac area of the AAA and from early diastole to end-diastole separation in flow lines are noted in a similar pattern of systole and are of higher velocity magnitude in the proximal rea of neck of AAA . Model_5, which is intrarenal saccular in shape AAA, has a neck angle $\alpha_1 = 35^0$, $\alpha_2 = 41^0$, it has been found that at T_0, the flow lines are negligible because of their saccular shape, early flow separation, and recirculation with vortex formation in the hull of the saccular aneurysms as seen which can be cross-validated with from (Figure 4.11) during early systole. With the accelerating phase of systole the flowlines are getting accumulated in the saccular portion of AAA due to which blood components get many disturbances in the flow dynamics; however, during the late diastole the flow separation and vortex formation, which get intensified during diastole/systole transition are noted. All of the models in the figure indicate that the impact of neck angle on flow fields is substantial. The AAA-neck angle can range from 0 to 90 degrees in clinical practice. The neck angle, as previously discussed, has a significant impact on flow patterns and wall-stress distributions in AAAs. A large neck angle can result in severe asymmetric geometries, disrupted flow patterns, and proximal wall stress concentrations. Furthermore, a large neck angle raises the possibility of stent graft migration or downward device movement if the AAA is fixed with a stent graft.

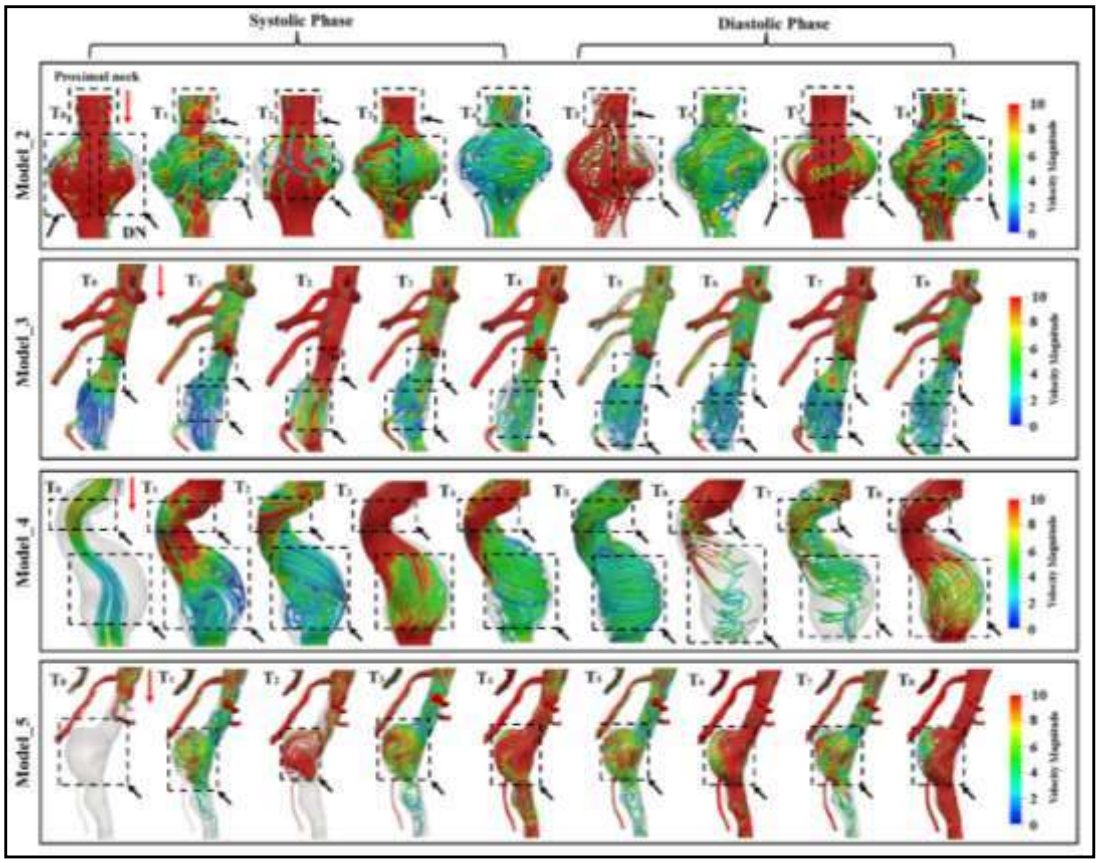

Figure 4.11 : Neck angle and aneurysm location effect on the 3D flow pattern in the diseased case of four models (Model_1, Model_2, Model_3 & Model_4) during the cardiac cycle. The blood flow is from top to bottom, marked with a red arrow.

4.3.4 Effect of bifurcation angle on flowlines

(Figure 4.12) depicts the influence of iliac bifurcation angle on streamlines of blood flow during a cardiac cycle in all four aortofemoral models. Aortic bifurcation angles of varying grades would increase the risk factor for aortic-iliac occlusive disease. The common iliac bifurcation angles measured in all four cases are $\theta_{1,2,3,4} = 47^0, 58^0, 65^0, 54^0$. In Model_2 with $\theta_2 = 47^0$ it is noted that during T_2 and T_4 in the systolic phase, flow lines are regular, and the length of streamlines attend fully, however during T_0, T_1, and T_3 in the systolic phase, the flow lines start getting irregular

patterns from the start of bifurcation angle to the bifurcated blood vessel. Also, during the diastolic phase, i.e., at $T_{5,a}$ reduction in flow lines with irregularity in the pattern is present; however, during T_6 and T_8, flow lines are of full length, but irregularity in the flow pattern is noted. In model_3 with $\theta_3 = 58^0$ it is observed that with an increase in the bifurcation angle, irregularity in flow lines formed and during the systolic phase, i.e., from ($T_0 - T_4$) it is found that during T_0 and T_2 a fraction of flow is trapped in the left internal iliac aneurysm present in the model just after the common iliac bifurcation. Also, during T_2, the mainstream from the start of bifurcations enters the iliac bifurcations and proceeds towards the distal end of both iliac bifurcations of the blood vessel with almost no disturbances in flow lines. However, during the diastolic phase, i.e. (T_5-T_8) it is seen that some reduction in progressive flow lines is noted, which is because of AAA and flow separation, while the start of diastole is because of low velocity and spatial variations. Also, in the right iliac bifurcation domain the flow lines are having high irregular patterns. Model_4 which is doubly tilted in aneurysms shape and having common iliac bifurcation angle is 65^0, which is larger than the other two above models at T_0 and T_6 reduction in flow lines is noted, and the amount of flow lines in right iliac artery is less compared to the left one; however, at the remaining cardiac instant of the cardiac cycle, it has been noted that blood flow lines are exhibiting uniform flow patterns. In model_5, which is saccular in shape, the bifurcation angle is $54^{0;}$ it has been seen that due to saccular morphology of aneurysms the flow lines show very different behavior at every instant of the cardiac cycle. During T_4, T_6 and T_8 the flow lines exhibit maximum magnitude behavior as shown in (Figure 4.12) however, many irregularities are noted at remaining time instances of the cardiac cycle. It has been seen from all models that a wider bifurcation angle seems to create the

hemodynamic conditions necessary for common iliac artery aneurysms CIAA progression and eventual rupture.

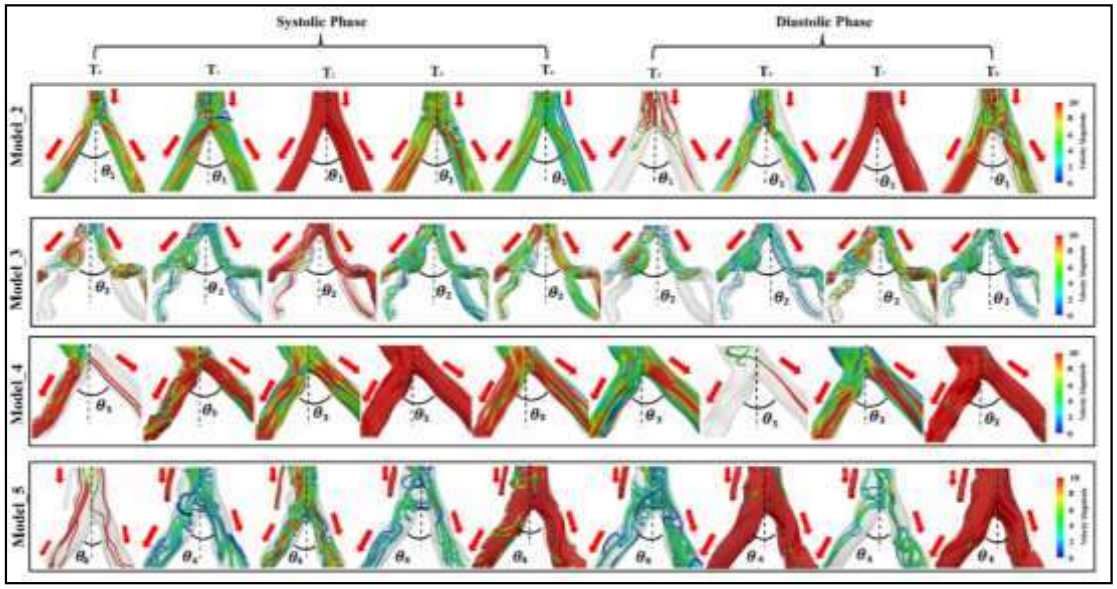

Figure 4.12 : Effect of iliac bifurcation angle on streamlines of blood flow during cardiac cycle

4.3.5 Effect of neck angle on wall shear stress

(Figure 4.13) depicts the effect of neck angle on WSS magnitude and their contour distribution in localized regions of aneurysm in all five aortofemoral models. The critical regions of WSS are highlighted by dotted curve box in (Figure 4.13). To see in details visualization of stress magnitude on wall surface, both view of the model (anterior and posterior view) has been considered. At cardiac instant T_1, which is the start of the systolic phase, it has been seen that in Model_2 and Model_4 at the top of aneurysm head high wall shear stress band is noted, which is highlighted by a dotted box in the (Figure 4.13); however, in model_5 in the anterior and posterior view of the blood vessel distributed WSS is noted which is highlighted by dotted box. At T_2 in model_5 many variations in WSS bands are noted near the distal end of the aneurysm,

as shown by the dotted box in the (Figure.4.13) at T_3 in Model_2 maximum wall shear stress zone is noted near the proximal and distal end of neck and toe of aneurysm, while in Model_4 just after first neck tilting high wall shear stress is noted on proximal head of the aneurysm, also at distal end of aneurysms in model_4 high wall shear stress zone is noted in anterior view of the blood vessel wall. During T_4 and T_5 only in model_5 high wall stress band is noted which is marked with doted box in the (Figure 4.13). During T_6 and T_7 the maximum localized wall shear stress area is marked with the dotted area in model_2, 4 and 5. Also during end of diastolic phase i.e. at T_8 maximum wall shear stress are noted in model_2, 3, 4 and 5 which is marked with the dotted area in the (Figure 4.13).

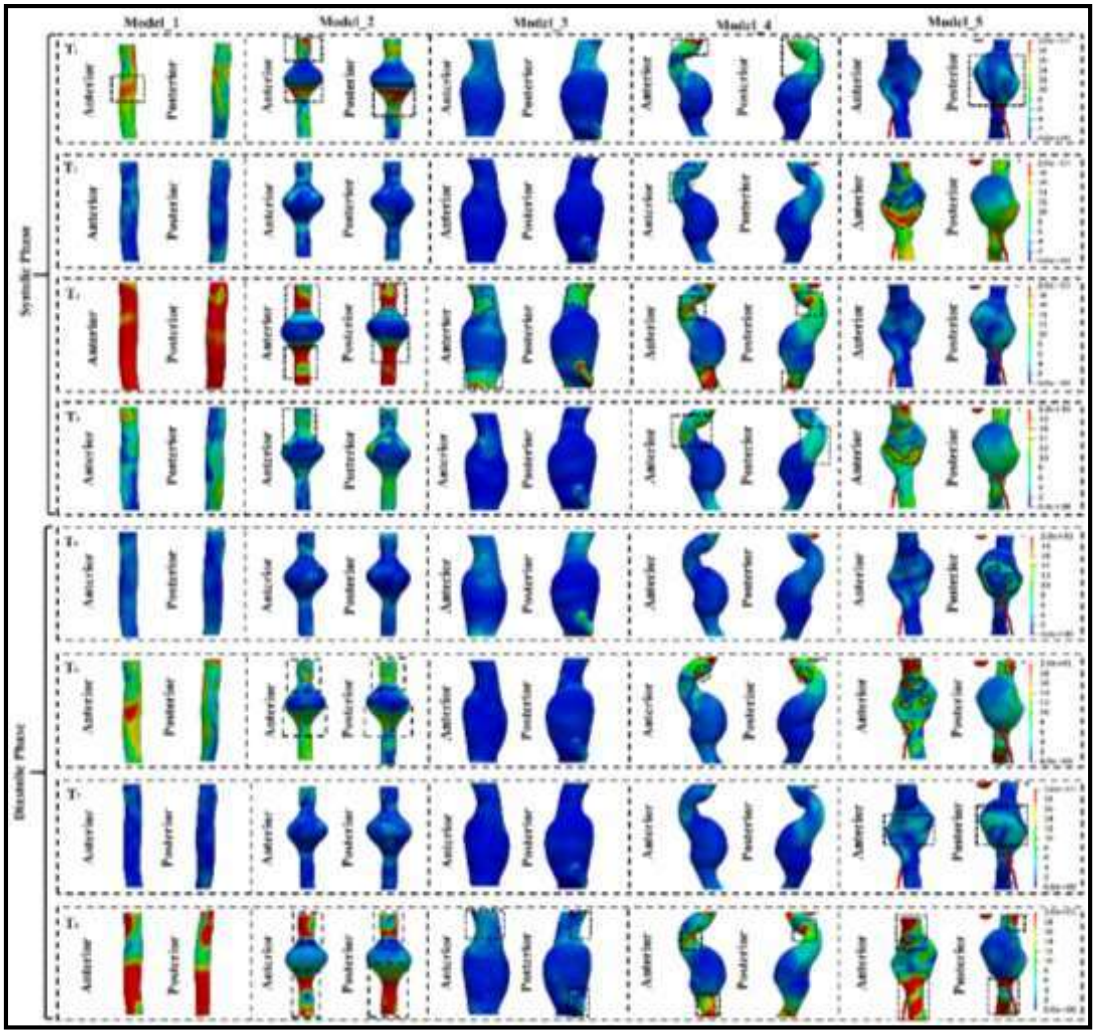

Figure 4.13 : Wall shear stress distribution in anterior and posterior view of all four aneurysm models of aortofemoral arteries in cardiac cycle.

4.3.6 Effect of aneurysm shape on hemodynamics parameters

4.3.6.1 TAWSS distribution

It is possible to extract the velocity and pressure fields as spatiotemporal data out from patient-specific CFD simulations. The shear stress-based characteristics can be used to produce a number of parameters of therapeutic interest. (Figure 4.14) shows time-averaged wall shear stress (TAWSS) contours for the five aortofemoral models at various dilation ratio and aneurysms location. With the increase in the dilation

maximum value of TAWSS also increases. The increase in TAWSS may be caused due to an increase in the instantaneous expansion ratio, which leads to an increase in the blood impingement velocity on the aneurysm dome, as discussed in earlier section. The area with low TAWSS is shown by a dark blue tint. Such situations are more prone to thrombus development and aneurysm wall thickening. According to prior investigations, the lower WSS area is similarly susceptible to rupture (Meng et al., 2014)(Lee et al., 2018).

4.3.6.2 OSI distribution

The OSI value explains how the direction of the WSS vector changes throughout a cardiac cycle. Higher values correspond to the recirculating region, whereas zero values are the region with no recirculation. (Figure 4.15) demonstrates the OSI contours for different shapes of abdominal aortic aneurysms. The maximum OSI area are marked with dotted box in the (Figure 4.15). Due to the recirculation that occurs as a result of curvature, the parent vessels that are curved have higher OSI values.

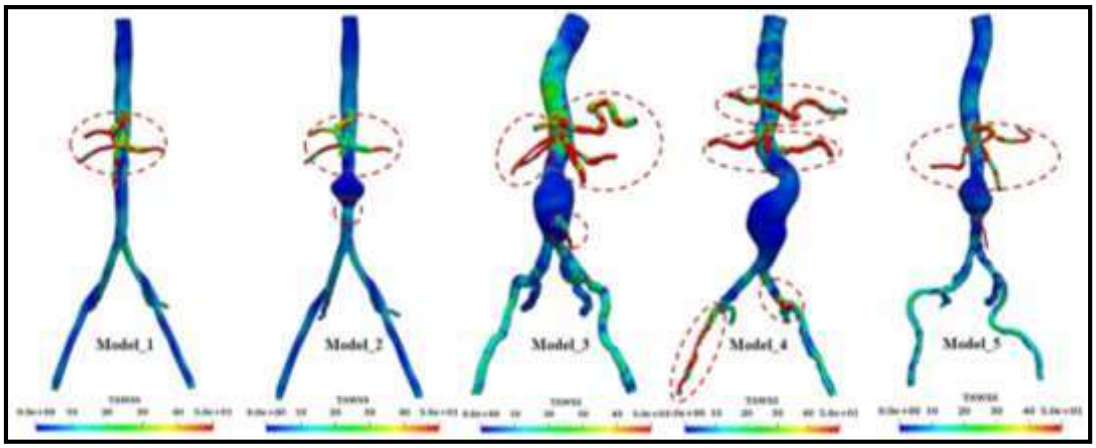

Figure 4.14 : Time average wall shear stress (TAWSS) contour in the five aortofemoral artery models

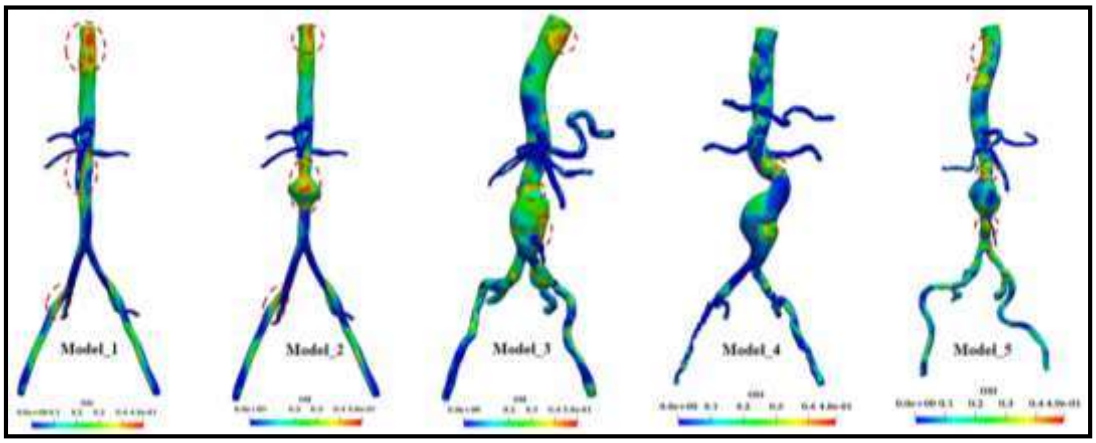

Figure 4.15 : Oscillatory shear index (OSI) contours in the five aortofemoral artery models considering various shapes of AAA.

4.3.6.3 Vortex distribution

It is crucial to examine the created vortices in order to better understand the dynamics of the vortex and how it interacts with the flow topology. In recent years, numerous studies have used the Q-criteria as a hemodynamic parameter (Cox and Plesniak, 2021; Seetharaman et al., 2021)(Kumar et al., 2022). (Figure 4.16) shows the three-dimensional vortex core region using Q-criteria and colored by the vorticity magnitude during peak systole of the cardiac cycle. It is noted from all four types of aortofemoral artery model under AAA conditions that across the neck region, vorticity magnitude is seen to be higher and in Model_2 and Model_5 magnitude of flow vorticity is higher because of localized shape effect in the arterial models.

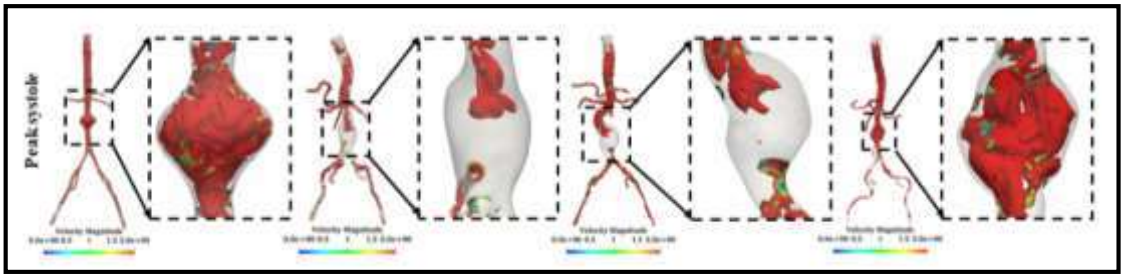

Figure 4.16 : The three-dimensional vortex core region using Q-criteria and colored by the vorticity magnitude in all four diseased models of aortofemoral artery

4.4 Summary

Utilizing multiple hemodynamic parameters and 3D vortex structures, the current study investigated the impact of AAA shape effect in terms of dilation, neck angle, common iliac bifurcation angle and aneurysms type on the prediction of aneurysm start and rupture. Unstable flow pattern, numerous vortices, high WSS bands neck proximal and distal end AAA in all four aortofemoral models are produced by an aneurysm, which results in oscillations in WSS, velocity waveform and flow rates. In the Future coupled fluid-structure interaction effects will be addressed more effectively by considering wall compliance under temporal pressure fluctuations and a suitable wall motion.

- It is noted from all models of AAA velocity distributions that the effect of aneurysm dilatation alters the flow velocity distribution, which may influence the lower extremities blood circulation.
- Flow separation occurs during systolic deceleration, and the vortex begins to travel in the aneurysm sac. In model_5, due to saccular in shape of aneurysm many

vortices start forming in the distal end of the aneurysm which can create thrombosis formation leading to rupture.

- A large neck angle can result in severe asymmetric geometries, disrupted flow patterns, and proximal wall stress concentrations. Furthermore, a large neck angle raises the possibility of stent graft migration or downward device movement if the AAA is fixed with a stent graft.
- It has been noted from bifurcation angle perspective that bifurcation angle creates the critical hemodynamic conditions necessary for common iliac artery aneurysms (CIAA) progression and eventual rupture.
- In Model_5 which is saccular type aneurysm, spiral flow lines are noted in saccular portion of the aneurysm which creates accumulation shear stress which helps in propagation on stress on the wall and may rupture the wall also.